metals

MDPI

Article

Nanoporous Microtubes via Oxidation and Reduction of Cu–Ni Commercial Wires

Emanuele Francesco Marano, Alberto Castellero * and Marcello Baricco

Department of Chemistry and NIS, University of Turin, I-10125 Turin, Italy;
emanuele.marano@unito.it (E.F.M.); marcello.baricco@unito.it (M.B.)
* Correspondence: alberto.castellero@unito.it; Tel.: +39-0116707097

Academic Editor: Houshang Alamdari
Received: 9 December 2016; Accepted: 29 January 2017; Published: 7 February 2017

Abstract: Metallic porous microtubes were obtained from commercial wires (200–250 µm diameter) of Cu-65Ni-2Fe, Cu-44Ni-1Mn and Cu-23Ni, alloys (wt. %) by surface oxidation at 1173 K in air, removal of the unoxidized core by chemical etching, and reduction in annealing in the hydrogen atmosphere. Transversal sections of the partially oxidized wires show a porous layered structure, with an external shell of CuO (about 10 µm thick) and an inner layer of NiO (70–80 µm thick). In partially oxidized Cu-44Ni-1Mn and Cu-23Ni, Cu_2O is dispersed in NiO because the maximum solubility of Cu in NiO is exceeded, whereas in Cu-65Ni-2Fe, a Cu_2O shell is present between CuO and NiO layers. Chemical etching removed the unoxidized metallic core and Cu_2O with formation of porous oxide microtubes. Porosity increases with Cu content because of the larger amount of Cu_2O in the partially oxidized wire. After reduction, the transversal sections of the metallic porous microtubes show a series of f.c.c.-(Cu,Ni) solid solutions with different compositions, due to the segregation of CuO and NiO during oxidation caused by the different diffusion coefficients of Ni and Cu in the respective oxides. Pore formation occurs at each step of the process because of the Kirkendall effect, selective phase removal and volume contraction.

Keywords: Cu-Ni alloy; oxidation; etching; reduction; porous material; microtube

---

1. Introduction

Microtubes and nanotubes attract interest both from the scientific and technological point of view because of the properties that allow their use as catalysts, sensors, drug-delivery carriers, acoustic insulators, biomedical diagnosis agents, and chemical reactors in Micro Electro Mechanical Systems (MEMS), lasers, magnetic, optical, semiconductor and biomedical devices [1–4]. In particular, metallic nanotubes attract attention because of magnetic properties [4], surface enhanced Raman scattering (SERS) [5] and catalytic performance [6]. The synthesis of microtubes and nanotubes is typically run by self-organization of constituent atoms or molecules, template-assisted method (assisted by electroless deposition, electrodeposition or atomic layer deposition), Kirkendall-based route or hydrothermal method [1,7–9].

Metallic porous materials are of great interest because of their functional and structural features. Due to their mechanical properties, metallic porous materials can solve the problem of intrinsic brittleness of ceramic materials [10,11]. Current applications of metallic porous materials are in the field of energy and environmental protection (e.g., vehicle exhaust gas, coal combustion) [12], in the chemical industry (e.g., microreactors) [13] and biomedical science (e.g., carrier of biological agents, bone and tissue substitute materials) [14]. Recently, Cu-Ni foam films [15] and nanoporous gold obtained from a metallic glass precursor [16] attracted attention because of the improved electrocatalitic activity and surface-enhanced Raman scattering, respectively.

In the case of metallic microtubes and nanotubes, the synthesis is usually performed by template method via electrochemical deposition [1,7,8,17]. This approach allows a fine tuning of the wall thickness and leads to the formation of compact and smooth surfaces. On the other hand, the fabrication of nanoporous microtubes is desirable because of the enhanced capillarity properties and the specific surface properties, which lead to potential applications in MEMS for fluid transportation or sensing [18–20].

The development of nanoporous materials, starting from the reduction of oxides, was investigated by several authors, and it is generally achieved by the selective removal of one phase by chemical routes [21,22]. In a previous work, a simple method for the synthesis of a nanoporous metallic microtube starting from a commercial constantan (Cu-Ni alloy) wire was presented [23]. The processing route consists of the following three steps: (1) partial oxidation of the alloy; (2) chemical etching for the removal of the un-oxidized inner core; and (3) reduction of the oxides in hydrogen atmosphere.

In this work, the same method was applied using commercial wires of Cu-Ni alloys with different Cu:Ni ratio and wires of the pure elements (i.e., Cu and Ni). The Cu/Ni ratio affects the phase selection and microstructure of the oxidized wires and leads to different levels of porosity in the final reduced microtubes.

2. Materials and Methods

Commercial wires of Cu (electrolytic copper, 99.9%), Ni (Alfa Aesar, Karlsruhe, Germany, 99.98%), Cu-65Ni-2Fe (Goodfellow, Huntingdon, UK), Cu-44Ni-1Mn (Gebauer & Griller, Vienna, Austria) and Cu-23Ni (MWS Wire Ind., Westlake Village, CA, USA) were used as starting materials. For the sake of simplicity, the alloys will be shortly named as Cu-65Ni, Cu-44Ni and Cu-23Ni, respectively. The diameter of the wires is 250 μm, except for Cu-44Ni-1Mn (200 μm).

In the first step, each wire was cut in 3–5 cm long pieces and placed in air in a pre-heated muffle oven at 1173 K inside alumina crucibles. In order to obtain similar oxide layers, the wires were exposed to the oxidation atmosphere for different times ranging from a minimum of 5 min to a maximum of 1440 min, on the basis of the composition.

In the second step, chemical etching with 65% nitric acid aqueous solution at room temperature allowed removal of the inner metallic core, together with some oxide phases, leaving intact the external oxide layer, with formation of an oxide microtube.

Finally, reduction of the microtubes was performed by heating the samples from room temperature up to 723 K at 10 K/min under 10 bar of hydrogen inside a High Pressure Differential Scanning Calorimeter (DSC) DSC HP-204 (Netzsch, Selb, Germany), using aluminium pans as sample holders.

Thermodynamic properties of the reactions involved were calculated using the Thermocalc software and the database "Substance" [24].

The thickness of the oxide layer after oxidation for different times was measured with a DMLM optical microscope (Leica, Wetzlar, Germany) across the transversal section of the samples. Scanning Electron Microscopy (SEM) observations were performed using a Stereoscan 410 (Leica, Wetzlar, Germany) equipped with an INCAx-sight probe (Oxford Instruments, Abingdon, UK) for Energy Dispersive X-ray analysis (EDX).

X-ray diffraction (XRD) measurements were performed with a X'Pert Pro (Cu Kα) (PANalytical B.V., Almelo, The Netherlands) using a capillary spinner technique with a 0.3 mm diameter glass capillary. Rietveld refinement was performed using the software MAUD (version 2.55 64 bit, Università degli Studi di Trento, Trento, Italy) [25]. The March–Dollase model was used to take preferential crystallographic reflections into account in the oxidized and chemically etched samples.

3. Results

3.1. Oxidation

Figure 1 shows the thickness of the oxide layer as a function of the square root of the time. Data points are calculated by averaging thickness measurements of the oxide in different positions in the same cross section and in different cross sections of the same sample. The error bars are the standard deviation of the averages. In the case of pure elements, a single linear behaviour is observed. In the case of Cu-Ni alloys, two oxidation steps are observed (continuous and dotted lines in Figure 1). Both steps can be described by a parabolic law, $x = \sqrt{K_p t}$ (where x, t and K_p are the oxide thickness, the oxidation time and the parabolic rate constant, respectively). As shown in Figure 1, the second oxidation step is faster than the first one and both oxidation steps become faster when the Ni content in the starting alloy decreases, in accordance with the literature [26–28]. K_p values for both steps are summarized in Table 1.

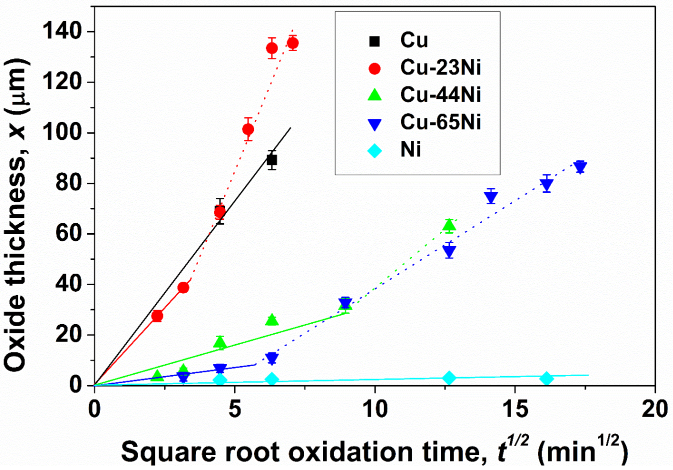

Figure 1. Oxide thickness as a function of the square root of oxidation time at 1173 K for Cu (black squares), Cu-23Ni (red circles), Cu-44Ni (green up triangles), Cu-65Ni (blue down triangles) and Ni (cyan diamonds) samples. In the case of pure elements, experimental points were fitted with a single parabolic law (continuous lines), $x = \sqrt{K_p t}$, where x, t and K_p are the oxide thickness, the oxidation time and the parabolic rate constant, respectively. In the case of Cu-Ni alloys, experimental points show the presence of two steps (continuous and dotted lines, respectively). For Cu-23Ni and Cu-65Ni samples, each step was fitted with a parabolic law, leading to different values of the constant rate, K_p' and K_p'', as reported in Table 1.

Table 1. Values of the parabolic rate constants at 1173 K for oxidation of Ni, Cu-65Ni, Cu-44Ni, Cu-23Ni and Cu samples. K_p' and K_p'' values are related to the first oxidation step (present in all the samples) and the second oxidation step (present only in the Cu-Ni alloys), respectively.

Sample	K_p' ($g^2 \cdot cm^{-4} \cdot s^{-1}$)	K_p'' ($g^2 \cdot cm^{-4} \cdot s^{-1}$)
Ni	1.62×10^{-9}	n.a.
Cu-65Ni	3.32×10^{-8}	6.40×10^{-7}
Cu-44Ni	1.64×10^{-7}	-
Cu-23Ni	2.00×10^{-6}	9.56×10^{-6}
Cu	2.83×10^{-6}	n.a.

According to Refs. [27–30], oxidation of Cu-Ni alloys occurs through several reactions. On one hand, Cu rapidly oxidizes to Cu(I), and, subsequently, it transforms to Cu(II) with a slower kinetics, forming an outer layer. On the other hand, an inner layer, consisting of a NiO and Cu_2O mixture, forms between the outer Cu(II) oxide layer and the metallic core.

The occurrence of two steps with different oxidation rates (see Figure 1 and Table 1) is due to the recrystallization of the outer CuO layer and to the stress relaxation of the inner layer [27]. Thus, diffusion of oxygen through anion vacancies in the inner layer becomes faster, leading to a larger macroscopic oxidation rate [27].

On the basis of the kinetic data, we tuned the oxidation time in order to obtain partially oxidized wires with similar oxide thickness (i.e., 80–100 μm) and obtain mechanically self-standing oxide layers. Thus, wires of Cu-23Ni, Cu-44Ni, Cu-65Ni and Cu were oxidized for 30 min, 160 min, 300 min and 1440 min, respectively. In the case of pure Ni, the oxidation kinetics is extremely slow as a consequence of passivation (see, for instance, Ref. [31]). Therefore, we decided to exclude this sample from the prosecution of the work.

Figure 2a shows the XRD patterns of the oxidized samples. The results of the Rietveld refinement related to the XRD patterns of Figure 2a are reported in Table 2. In the case of pure copper, oxidation for 1440 min leads to the formation of Cu_2O and CuO. In the case of Cu-23Ni and Cu-44Ni (oxidized for 30 min and 160 min, respectively), the following phases can be identified: Cu_2O, CuO and NiO. As expected, the amount of copper oxides (i.e., Cu_2O, CuO) increases as the Cu content in the starting alloy increases. Finally, in the case of Cu-65Ni, oxidized for 300 min, the main phases are CuO and NiO. A residual amount of the unoxidized f.c.c.-(Cu-Ni) starting alloy is present due to the slower kinetics of oxidation for this alloy (Figure 1 and Table 1), while the amount of Cu_2O is below the detection limit of the technique.

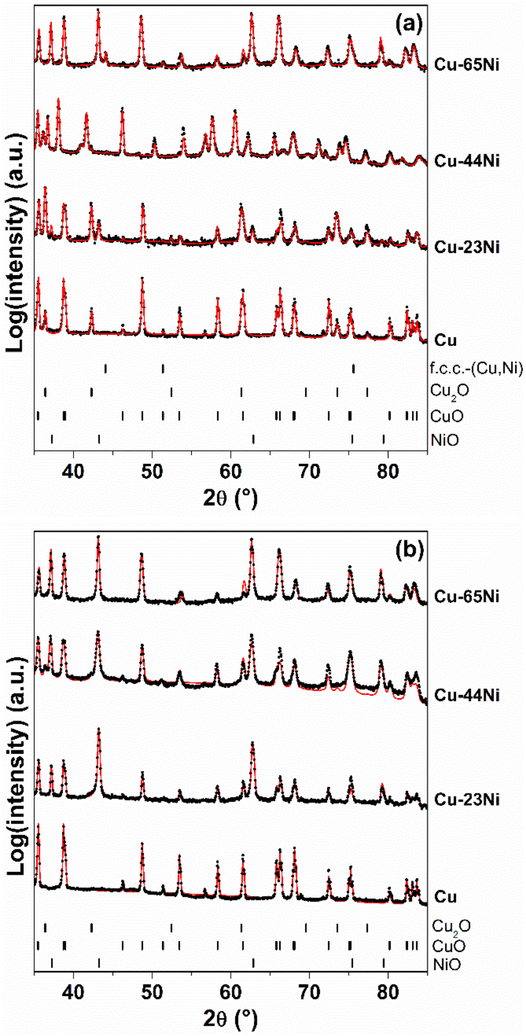

Figure 2. *Cont.*

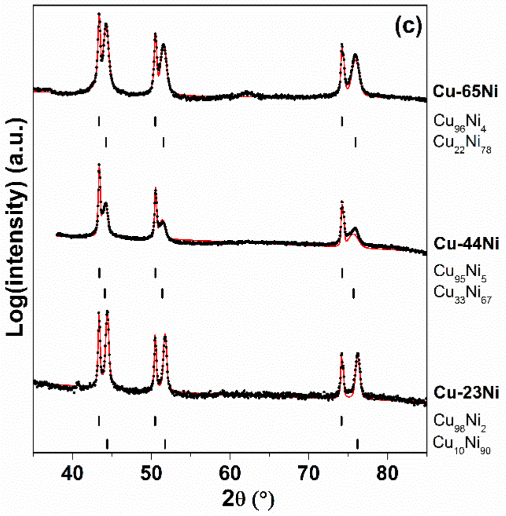

Figure 2. X-ray diffraction (XRD) patterns of partially oxidized wires (**a**); oxide microtubes obtained after chemical etching of the partially oxidized wires (**b**); metallic microtubes obtained after reduction of the oxide microtubes (**c**) for Cu-65Ni, Cu-44Ni, Cu-23Ni and Cu samples. Black dots and red lines represent experimental points and refined patterns, respectively. Vertical lines at the bottom of each figure indicate the positions of the crystallographic reflections for the different phases.

Table 2. Quantitative phase analysis (wt. %) and corresponding lattice parameters of Cu-65Ni, Cu-44Ni, Cu-23Ni and Cu samples after oxidation, chemical etching and reduction, obtained by Rietveld refinement of the X-ray diffraction (XRD) patterns shown in Figure 2.

Sample	Process Step	Quantitative Phase Analysis (wt. %)	Lattice Parameters
Cu-65Ni	Oxidation (300 min)	CuO: 42% NiO: 47% f.c.c.-(Cu,Ni): 11%	*a* = 0.47045 nm, *b* = 0.34077 nm, *c* = 0.51340 nm, β = 99.6° *a* = 0.41923 nm *a* = 0.35565 nm
	Etching	CuO: 29% NiO: 71%	*a* = 0.47043 nm, *b* = 0.34047 nm, *c* = 0.51234 nm, β = 99.6° *a* = 0.41914 nm
	Reduction	f.c.c.-(Cu rich): 37% f.c.c.-(Ni rich): 63%	*a* = 0.36108 nm *a* = 0.35436 nm
Cu-44Ni	Oxidation (160 min)	Cu_2O: 7% CuO: 58% NiO: 35%	*a* = 0.42696 nm *a* = 0.46980 nm, *b* = 0.34110 nm, *c* = 0.51332 nm, β = 99.4° *a* = 0.41920 nm
	Etching	Cu_2O: 3% CuO: 43% NiO: 54%	*a* = 0.42696 nm *a* = 0.46884 nm, *b* = 0.34202 nm, *c* = 0.51307 nm, β = 99.4° *a* = 0.41913 nm
	Reduction	f.c.c.-(Cu rich): 52% f.c.c.-(Ni rich): 48%	*a* = 0.36102 nm *a* = 0.35538 nm
Cu-23Ni	Oxidation (30 min)	Cu_2O: 43% CuO: 48% NiO: 9%	*a* = 0.42722 nm *a* = 0.46824 nm, *b* = 0.34181 nm, *c* = 0.51274 nm, β = 99.4° *a* = 0.41841 nm
	Etching	CuO: 25% NiO: 75%	*a* = 0.46846 nm, *b* = 0.34214 nm, *c* = 0.51289 nm, β = 99.5° *a* = 0.41839 nm
	Reduction	f.c.c.-(Cu rich): 31% f.c.c.-(Ni rich): 69%	*a* = 0.36131 nm *a* = 0.35328 nm
Cu	Oxidation (1440 min)	Cu_2O: 8% CuO: 92%	*a* = 0.42685 nm *a* = 0.46835 nm, *b* = 0.34235 nm, *c* = 0.51293 nm, β = 99.5°
	Etching	CuO: 100%	*a* = 0.46848 nm, *b* = 0.34390 nm, *c* = 0.51308 nm, β = 99.5°

Figure 3a–d shows the SEM micrographs (backscattered electron detector) of the transversal cross sections of the oxidized wires. In the case of Cu-23Ni, Cu-44Ni and Cu-65 Ni, the cross section of the

partially oxidized wires reveals the presence of an external darker oxide layer and an internal brighter unoxidized metallic core. In the case of fully oxidized Cu, Figure 3d, concentric layers of two oxides are visible. As mentioned before, Cu rapidly oxidizes to Cu(I), and, subsequently, it transforms to Cu(II) with a slower kinetics. Thus, in agreement with the XRD patterns, Figure 2a, and the compositional contrast, the external layer can be related to CuO, whereas the internal one can be related to Cu_2O.

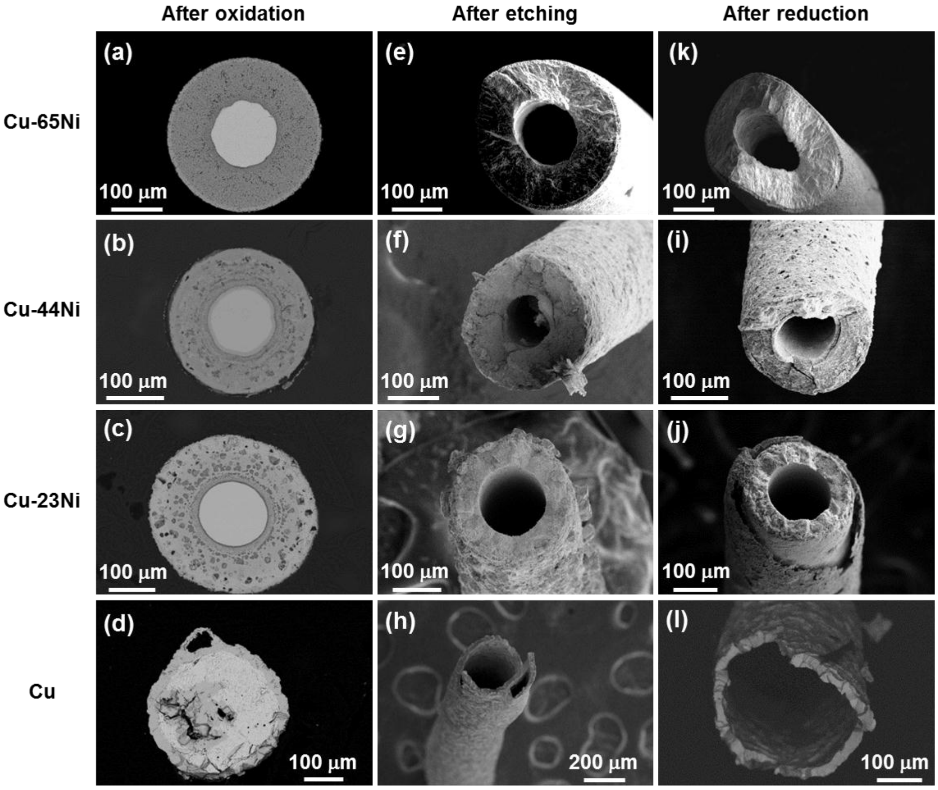

Figure 3. Backscattered electrons images of the cross section of the oxidized wires: (**a**) Cu-65Ni; (**b**) Cu-44Ni; (**c**) Cu-23Ni; (**d**) Cu. Secondary electron SEM images of the oxide microtubes obtained after chemical etching of the oxidized wires: (**e**) Cu-65Ni; (**f**) Cu-44Ni; (**g**) Cu-23Ni; and (**h**) Cu. Secondary electron SEM images of the metallic microtubes obtained after reduction of the oxide microtubes: (**k**) Cu-65Ni; (**i**) Cu-44Ni; (**j**) Cu-23Ni; and (**l**) Cu.

Figure 4a–c shows magnified views of the cross sections reported in Figure 3a–c, respectively, together with the corresponding EDX map. All the three partially oxidized alloys show a Cu-rich external oxide layer (red pixels) that corresponds to CuO which is detected in the corresponding XRD patterns. The intermediate oxide layers of the three samples show a different contrast of red and green pixels corresponding to Cu and Ni, respectively. In Cu-65Ni, an almost uniform green intermediate oxide layer is observed, Figure 4a, suggesting the presence of almost only NiO, in accordance with the XRD results, Figure 2a. In Cu-44Ni and Cu-23Ni, the intermediate oxide layer shows a mixture of green and red pixels, indicating the coexistence of NiO and Cu_2O in agreement with the corresponding XRD patterns. In the case of Cu-65Ni, Figure 4a, and Cu-44Ni, Figure 4b, between the intermediate oxide layer and the unoxidized metallic core, there is a thin red ring (Cu-rich), which has a metallic appearance when observed at the optical microscope [23]. The formation of this metallic copper layer occurs according to the reaction [29]:

$$Cu_2O + Ni \rightarrow 2Cu + NiO \quad (1)$$

which is spontaneous at 1173 K ($\Delta G = -51.3$ kJ/mol).

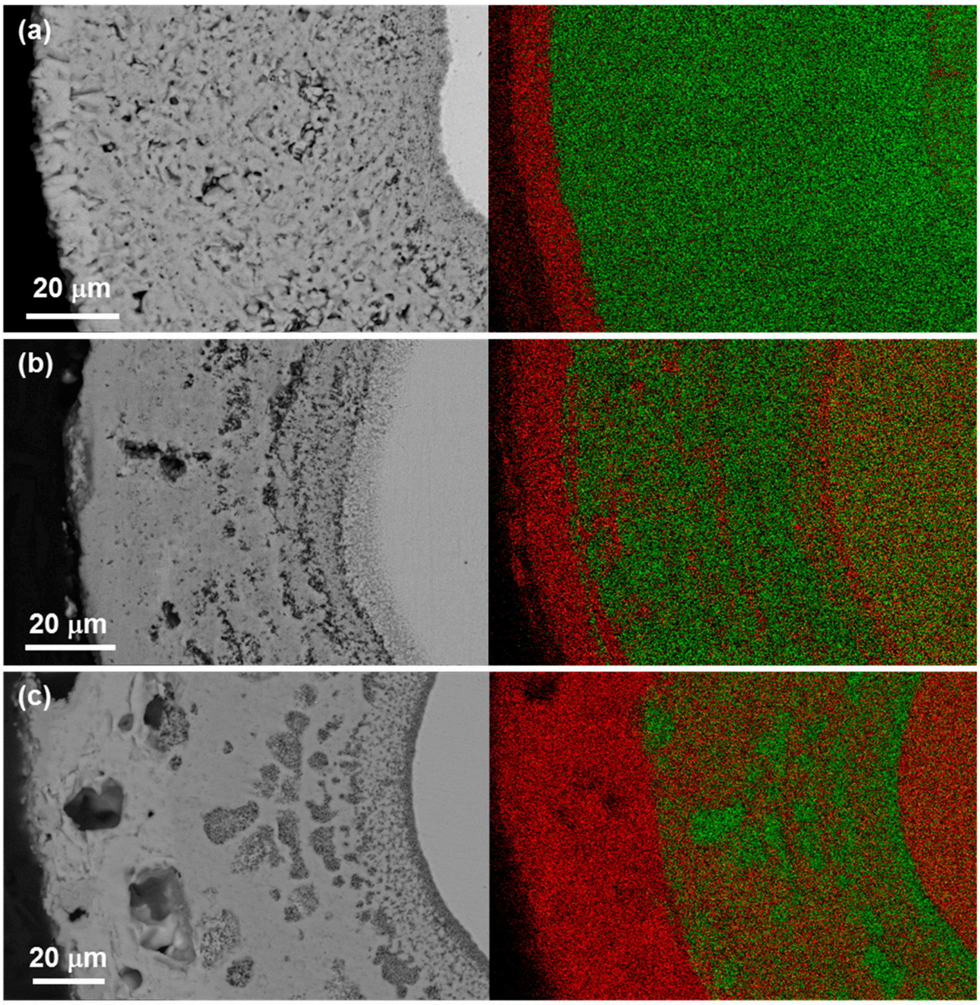

Figure 4. Backscattered electron micrographs (**left**) and elemental maps (**right**) of the cross section of the oxidized Cu-65Ni (**a**); Cu-44Ni (**b**) and Cu-23Ni (**c**) wires. In the elemental maps, red and green dots indicate Cu and Ni, respectively.

Figure 5a shows the composition profiles of the cross sections of the partially oxidized wires (Figure 4). In the case of Cu-65Ni (red circles), the abrupt decrease of Cu content corresponds to the sharp transition between the thin external CuO layer and the intermediate Ni-rich oxide layer, Figure 4a. The amount of Cu in the Ni-rich oxide layer ranges between 3 at. % and 28 at. %. On the basis of the lattice parameter (a = 0.41923 nm) and the Vegard law for $Ni_{1-x}Cu_xO$ [32], an average content around 25 at. % of Cu in NiO can be estimated. According to Ref. [33], the maximum solubility of Cu in NiO is about 25 at. %; therefore, it can be concluded that the intermediate Ni-rich oxide layer consists of almost only (Cu,Ni)O. Finally, the rapid increase of Cu content at an oxide/metal interface corresponds to the thin metallic copper ring observed in Figure 4a. In the case of Cu-44Ni (black triangles), a similar profile is observed. However, the amount of Cu in the Ni-rich oxide is above the solubility limit, leading to the precipitation Cu_2O particles and their coexistence with NiO in the intermediate Ni-rich oxide layer, as confirmed by the green and red regions in Figure 4b and by the XRD patterns, Figure 2a, respectively. The occurrence of a saturated (Cu,Ni)O solid solution is supported by the value of the lattice parameter (a = 0.41920 nm), which corresponds to about 25 at. % of Cu. Finally, in the case of Cu-23Ni (green squares), the profile shows a thicker Cu-rich layer, corresponding to the external CuO ring, followed by an intermediate layer with a copper content between 45 at. % and 60 at. %. In this case, the value of the lattice parameter is 0.41841 nm, which corresponds to about 13 at. % of Cu (i.e., below the solubility limit of (Cu,Ni)O). Thus, the intermediate oxide layer contains a larger amount of Cu_2O with respect to the other two samples, as shown by the red/green contrast in Figure 4 and in accordance with the quantitative analysis of the XRD patterns (Table 1).

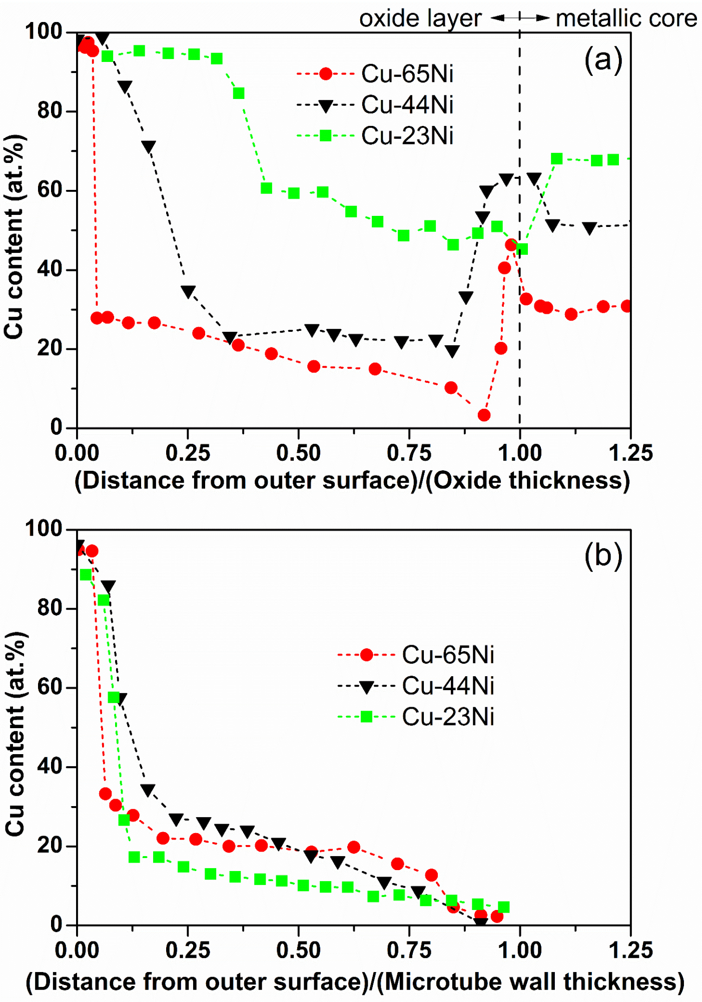

Figure 5. Energy Dispersive X-ray analysis (EDX) composition profiles of Cu as a function of the distance from the outer surface for the partially oxidized wires (**a**) and the reduced metallic microtubes (**b**). Red circles, black triangles and green squares refer to Cu-65Ni, Cu-44Ni and Cu-23Ni samples, respectively. Dashed lines are a guide to the eye.

3.2. Etching

Figure 2b shows the XRD patterns of the samples after etching with HNO_3 solution. The corresponding quantitative analysis of the crystalline phases is reported in Table 1. In the case of pure Cu sample, only the reflections of CuO are observed whereas the peaks of Cu_2O disappear. The dissolution of Cu_2O leads to the formation of an oxide microtube formed by the external layer of CuO, which is unaffected by the HNO_3 attack, Figure 3h. In the case of Cu-Ni samples, XRD patterns show the presence of CuO and NiO, while the peaks of Cu_2O and residual f.c.c. solid solutions disappear. Thus, microtubes with two concentric layers of CuO (external) and (Cu,Ni)O (internal) are obtained (Figure 3e–g).

3.3. Reduction

Figure 6 shows the HP-DSC traces related to the reduction of Cu, Cu-23Ni, Cu-44Ni and Cu-65Ni.

In the case of Cu, a single broad exothermic signal, starting around 440 K, is visible. In the case of the Cu-Ni samples, the onset temperature of the first sharp peak (indicated by the arrows on the left in Figure 6) increases with the Ni content (from 460 K for Cu-23Ni and Cu-44Ni to 510 K for Cu-65Ni). In some cases (i.e., Cu-23Ni and Cu-44Ni), the first signal is split into two overlapped peaks. The splitting of the first peak can be likely due to the inhomogeneous morphology of the oxide layer (Figure 4), which can affect the kinetics of the reduction reaction. After the main sharp peak, a second broad exothermic signal (indicated by the arrows on the right in Figure 6) appears around 550 K, which is absent in the reduction of the pure Cu sample. XRD analysis (not shown) performed before and after the beginning of the second broad DSC signal reveal that the first sharp double signal is related to the reduction of CuO, while the second broad signal around 550 K corresponds to the reduction of NiO.

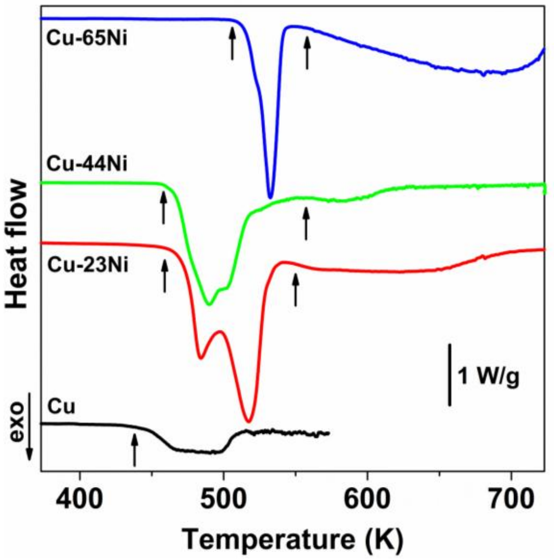

Figure 6. High Pressure Differential Scanning Calorimetry (HP-DSC) traces of the oxide microtubes under hydrogen atmosphere.

Figure 2c shows the XRD patterns of the samples after reduction in H_2 atmosphere. Obviously, in the case of Cu sample, only the diffraction peaks of Cu (f.c.c.) are present (not shown). In the case of Cu-Ni samples, reflections of two f.c.c. solid solutions (Cu- and Ni- rich, respectively) are observed. The crystallographic reflections of the Ni-rich f.c.c. solid solution appear broader than those corresponding to the Cu-rich f.c.c. solid solution. The morphology of metallic microtubes obtained after reduction is shown in Figure 3k–l. In the case of Cu-65Ni and Cu-44Ni samples, Figure 2k,i, respectively, uniform microtubes are obtained, while, in the case of Cu-23Ni wire, Figure 3j, two concentric microtubes are obtained. Figure 5b shows the composition profile of the microtubes shown in Figure 3k–j. In all of the samples, the observed progressive decrease of the Cu content from the external surface, which consists of almost pure copper, towards the internal surface, which consists of almost pure nickel, derives from the multi-layered oxide structure. In the case of Cu-23Ni, the external and internal microtubes are Cu- and Ni- rich, respectively. In this sample, the external microtubes can be detached from the internal one, so that an Ni-rich microtube is obtained, as shown in Figure 7. The red pixels indicate the presence of residual copper on the surface of the Ni-rich microtube.

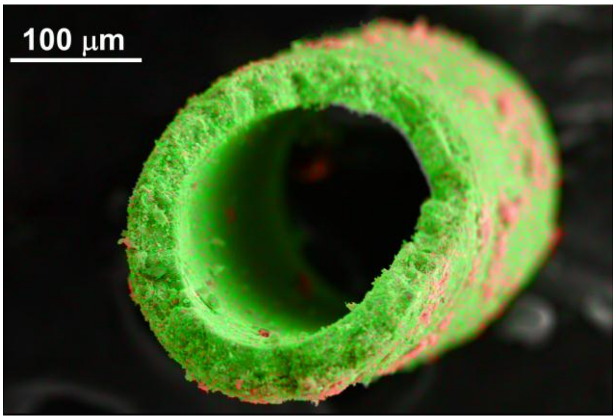

Figure 7. Secondary electrons image and EDX map of the Ni-rich microtube obtained after detachment of the external Cu-rich microtube.

The compositional gradient of the reduced microtubes, Figure 5b, shows the presence of a series of f.c.c.-(Cu-Ni) solid solutions with different compositions. As shown in Ref. [23] for the Cu-44Ni sample, the broad crystallographic reflections of the Ni-rich f.c.c. solid solution can be successfully fitted by Rietveld refinement assuming the coexistence of various f.c.c.-(Cu-Ni) solid solutions with different lattice parameters, as a consequence of the continuous variation in composition along the cross section of the microtubes. On the basis of the experimental results in Figures 2c and 5b, the same explanation can be given for the broadening of the crystallographic reflections of the Ni-rich f.c.c. solid solution in Cu-23Ni and Cu65-Ni samples. Thus, the values of the lattice parameters reported for the Ni-rich f.c.c. solid solution in Table 1 are just representing an average value of the lattice parameters of the various solid solutions with different composition.

The morphology of internal walls of the obtained microtubes show different features, depending on the composition of the starting alloy. In Cu-65Ni, Figure 8a, the metallic particles have irregular shapes, whereas in Cu-44Ni, Figure 8b, the shape of the metallic particles becomes smoother. In both samples, the size of the metallic particles is similar (average size of 280 ± 90 nm and 270 ± 70 nm for Cu-65Ni and Cu-44Ni, respectively). They appear isolated and not interconnected pores are visible between the metallic particles on the surface. In the case of Cu-23Ni, the internal surface is characterized by interconnected pores separated by metallic ligaments, as shown in Figure 8c. In this case, the ligament width is 430 ± 100 nm and the pore size is 280 ± 80 nm.

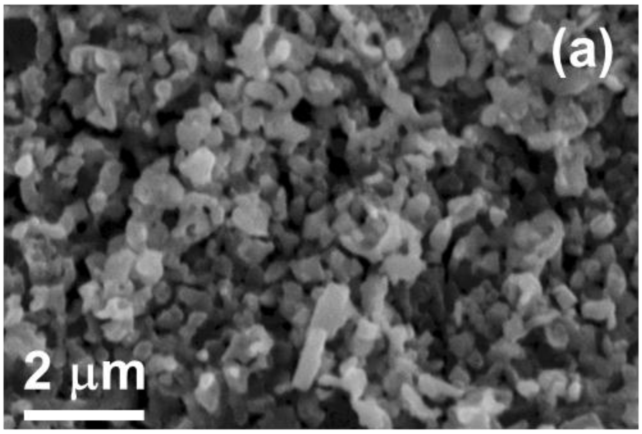

Figure 8. *Cont.*

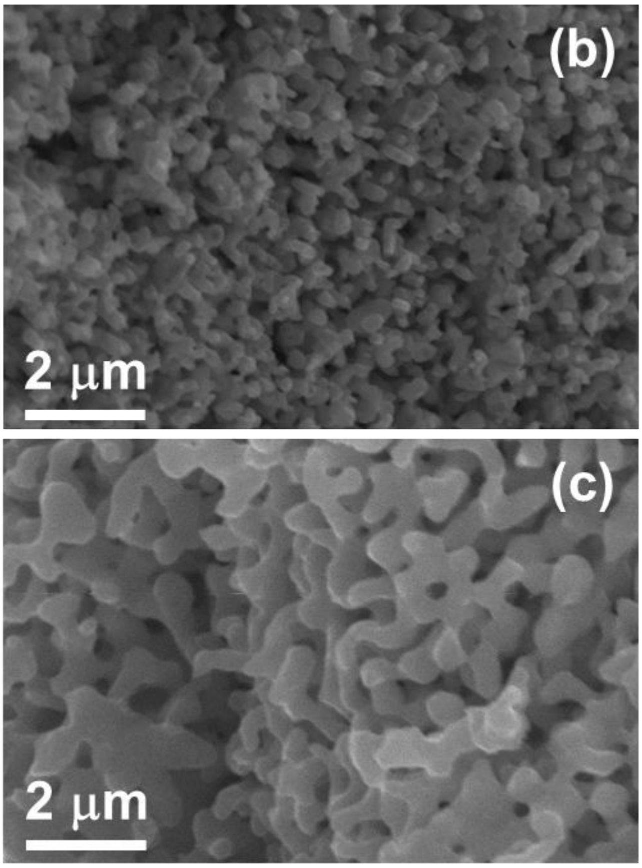

Figure 8. Secondary electrons images of the inner porous region in the reduced metallic microtubes: (**a**) Cu-65Ni; (**b**) Cu-44Ni; (**c**) Cu-23Ni.

4. Discussion

Figure 9 shows a scheme of the cross section of the wires of the different alloys after oxidation, etching and reduction, based on the experimental results presented in the previous sections. In all cases, after oxidation, the external layer consists of CuO. Only in the case of Cu-23Ni, a pure Cu_2O layer is present beneath the external CuO layer. Subsequently, in all samples, a mixed layer consisting of (Ni,Cu)O and Cu_2O is observed, where the amount of Cu_2O increases as the Cu content of the alloy increases. Finally, between the (Ni,Cu)O + Cu_2O oxidized layer and the unoxidized metallic core, a thin metallic ring containing pure Cu is observed in Cu-65Ni and Cu-44Ni. According to the literature [28], the Cu ring is expected to also be present in Cu-23Ni; however, it cannot be detected in the EDX map, Figure 4c, and the composition profile, Figure 5b. A possible explanation is that the results of the EDX microprobe are affected by the surrounding matrix: the small composition difference between the unoxidized metallic core and the expected Cu ring likely leads to a limited contrast between these two regions in the EDX map.

After oxidation, all of the Cu-Ni samples show some degree of porosity. Cu and Ni are segregated during oxidation of Cu-Ni alloys as a consequence of the larger diffusion coefficient of Cu in Cu_2O with respect to the one of Ni in NiO [34]. The different mobility of the metallic ions in the corresponding oxides creates an excess of vacancies that coalesce, with consequent formation of pores by the Kirkendall effect [35].

After chemical etching of the partially oxidized wires, the unoxidized metallic core and Cu_2O are leached and a self-standing oxide microtube is obtained. The removal of Cu_2O from the (Ni,Cu)O matrix induces the formation of further porosity. The formation of pores is proportional to the Cu_2O content in the alloy (Cu-23Ni > Cu-44Ni > Cu-65Ni). In the case of the Cu-23Ni sample, the amount of Cu dissolved in (Ni,Cu)O (13 at. %) is lower than the one foreseen by the equilibrium. This is likely due to kinetic reasons, since the oxidation time (30 min) is probably not enough to complete the solubilisation of Cu ions in (Ni,Cu)O, leaving an amount of Cu_2O larger than expected in equilibrium conditions. Additional porosity forms during reduction because of the contraction due to the different densities of f.c.c. Cu-Ni solid solutions (8.9 g/cm^3) and Cu-Ni-oxides (about 6.5 g/cm^3).

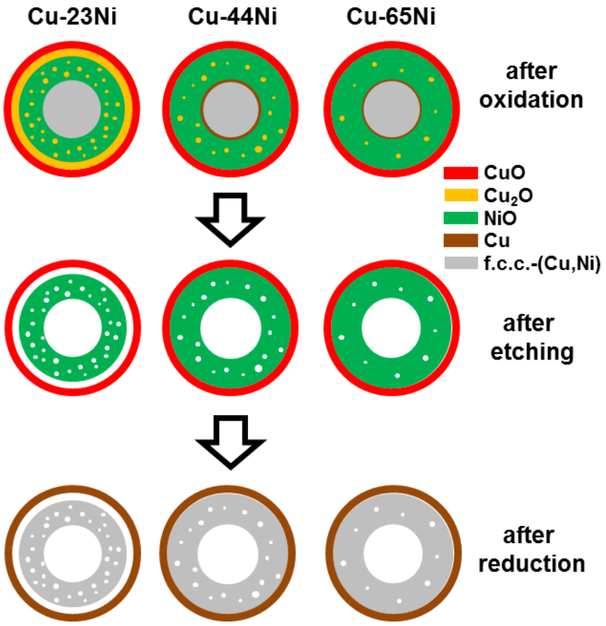

Figure 9. Scheme of the cross section of the partially oxidized wires (top), the oxide microtubes after chemical etching (middle) and metallic microtubes obtained after reduction under hydrogen atmosphere (bottom). Legend of the phases: CuO (red), Cu_2O (yellow), NiO (green), Cu (brown), and f.c.c.-(Cu,Ni) (grey).

The morphology of the inner wall of the reduced microtubes depends on the Cu-content in the starting alloy and the relative amount of Cu_2O in the partially oxidized wire. In the case of de-alloying of metallic alloys, interconnected porosity forms when the most noble element is below the "parting limit", so that, after removal of the less noble elements, the most noble element atoms reorganize themselves by surface diffusion forming hillocks separated by pores [36,37]. In our case, the selective etching of a compound (i.e., Cu_2O) in a corrosion resistant matrix, (Ni,Cu)O, is carried out. Only, in Cu-23Ni, the amount of Cu_2O is larger than the one of (Ni,Cu)O (see Table 1) to allow the percolation of the etching agent through the (Ni,Cu)O matrix, leaving a continuous network of interconnected ligaments and pores, as shown in Figure 8c. In the case of Cu-44Ni, the presence of rounded metallic particles on the internal surface of the reduced microtube, Figure 8b suggests the occurrence of surface diffusion of the atoms in the (Ni,Cu)O matrix. However, the amount of Cu_2O is lower than the one of (Cu,Ni)O (see Table 1), thus no interconnected ligaments and pores form. Finally, in the case of Cu-65Ni, the very low amount of Cu_2O with respect to (Cu,Ni)O (below the detection limit of X-ray diffraction) is not enough to promote the reorganization of the atoms in the (Cu,Ni)O matrix by surface diffusion, leaving particles with irregular shapes, as shown in Figure 8a.

5. Conclusions

In this work, porous metallic microtubes were obtained by partial oxidation of Cu-Ni wires with different composition (Cu-23Ni, Cu-44Ni, Cu-65Ni), chemical etching of the partially oxidized wires and reduction of the oxide microtubes.

In all samples, after oxidation, the external layer consists of CuO and the internal oxide layer is a mixture of Cu_2O and NiO. Only in the Cu-23Ni sample is a layer of pure Cu_2O present between the CuO and the Cu_2O/NiO layers. Furthermore, the amount of Cu_2O increases as the amount of Cu in the starting alloy increases.

In the etching step, the unoxidized metallic core and Cu_2O are selectively removed, leaving a porous oxide microtube, where the external and internal layers are CuO and NiO, respectively.

In the final step, the oxide microtube is reduced to a metallic microtube. In the case of Cu-44Ni and Cu-65Ni wires, the microtube section presents a continuous concentration gradient, which shows an increase of the Ni content from the outer wall towards the inner wall. In the case of the Cu-23Ni sample, two concentric and separated microtubes, respectively, rich in Cu and Ni, form because of the dissolution of the intermediate Cu_2O layer. In this way, a microtube of almost pure Ni can be obtained starting from a Cu-rich alloy.

Finally, the porosity of the metallic microtubes depends on the amount of Cu_2O formed during the oxidation step. Only in the case of the Cu-23Ni sample is the amount of the corrosion resistant NiO below the "parting limit", leading to the development of a continuous network of interconnected ligaments and pores by leaching of Cu_2O.

Author Contributions: A.C. and M.B. devised the experiments, E.F.M. performed the experiments and analysed the data, E.F.M., A.C. and M.B. discussed the data, E.F.M. wrote the manuscript, and A.C. and M.B. revised the manuscript.

Conflicts of Interest: The authors declare no conflict of interest.

References

1. Ye, Y.; Geng, B. Magnetic Nanotubes: Synthesis, Properties, and Applications. *Crit. Rev. Solid State Mater. Sci.* **2012**, *37*, 75–93. [CrossRef]
2. Chatzipirpiridis, G.; Ergeneman, O.; Pokki, J.; Ullrich, F.; Fusco, S.; Ortega, J.A.; Sivaraman, K.M.; Nelson, B.J.; Pané, S. Electroforming of implantable tubular magnetic microrobots for wireless ophthalmologic applications. *Adv. Healthc. Mater.* **2015**, *4*, 209–214. [CrossRef] [PubMed]
3. Chatzipirpiridis, G.; Avilla, E.; Ergeneman, O.; Nelson, B.J.; Pané, S. Electroforming of magnetic microtubes for microrobotic applications. *IEEE Trans. Magn.* **2014**, *50*, 5400403. [CrossRef]
4. Sui, Y.C.; Skomski, R.; Sorge, K.D.; Sellmyer, D.J. Nanotube magnetism. *Appl. Phys. Lett.* **2004**, *84*, 1525–1527. [CrossRef]
5. Zhou, H.; Zhang, Z.; Jiang, C.; Guan, G.; Zhang, K.; Mei, Q.; Liu, R.; Wang, S. Trinitrotoluene explosive lights up ultrahigh Raman scattering of nonresonant molecule on a top-closed silver nanotube array. *Anal. Chem.* **2011**, *83*, 6913–6917. [CrossRef] [PubMed]
6. Sanchez-Castillo, M.A.; Couto, C.; Kim, W.B.; Dumesic, J.A. Gold-Nanotube Membranes for the Oxidation of CO at Gas–Water Interfaces. *Angew. Chem. Int. Edit.* **2004**, *43*, 1140–1142. [CrossRef] [PubMed]
7. Rao, C.N.R.; Govindaraj, A. Synthesis of Inorganic Nanotubes. *Adv. Mater.* **2009**, *21*, 4208–4233. [CrossRef]
8. Cao, G.; Liu, D. Template-based synthesis of nanorod, nanowire, and nanotube arrays. *Adv. Colloid Interface Sci.* **2008**, *136*, 45–64. [CrossRef] [PubMed]
9. Kijima, T. Introduction to inorganic and metallic nanotubes. In *Inorganic and Metallic Nanotubular Materials: Recent Technologies and Applications*; Topics in Applied Physics; Kijima, T., Ed.; Springer: Berlin/Heidelberg, Germany, 2010; Volume 117, pp. 1–16.
10. Pia, G.; Delogu, F. Mechanical Properties of Nanoporous Au: From Empirical Evidence to Phenomenological Modeling. *Metals* **2015**, *5*, 1665–1694. [CrossRef]
11. Qin, J.; Chen, Q.; Yang, C.; Huang, Y. Research process on property and application of metal porous materials. *J. Alloy. Compd.* **2016**, *654*, 39–44. [CrossRef]
12. Qiu, G.; Xiao, J.; Zhu, J. Research history, classification and applications of metal porous metals. *J. Metal. Int.* **2013**, *18*, 70–73.
13. Hereijgers, J.; Desmet, G.; Breugelmans, T.; de Malsche, W. Strategies to integrate porous layers in microfluidic devices. *Microelectron. Eng.* **2015**, *132*, 1–13. [CrossRef]

14. Wu, S.; Liu, X.; Yeung, K.W.K.; Liu, C.; Yang, X. Biomimetic porous scaffolds for bone tissue engineering. *Mater. Sci. Eng. R* **2014**, *80*, 1–36. [CrossRef]
15. Zhang, J.; Baró, M.D.; Pellicer, E.; Sort, J. Electrodeposition of magnetic, superhydrophobic, non-stick, two-phase Cu-Ni foam films and their enhanced performance for hydrogen evolution reaction in alkaline water media. *Nanoscale* **2014**, *6*, 12490–12499. [CrossRef] [PubMed]
16. Scaglione, F.; Paschalidou, E.M.; Rizzi, P.; Bordiga, S.; Battezzati, L. Nanoporous gold obtained from a metallic glass precursor used as substrate for surface-enhanced Raman scattering. *Philos. Mag. Lett.* **2015**, *95*, 474–482. [CrossRef]
17. Brumlik, C.J.; Martin, C.R. Template synthesis of metal microtubules. *J. Am. Chem. Soc.* **1991**, *113*, 3174–3175. [CrossRef]
18. Lelea, D.; Nishio, S.; Takano, K. The experimental research on microtube heat transfer and fluid flow of distilled water. *Int. J. Heat Mass Transf.* **2004**, *47*, 2817–2830. [CrossRef]
19. Mondal, S.; De, S. Effects of non-Newtonian power law rheology on mass transport of a neutral solute for electro-osmotic flow in a porous microtube. *Biomicrofluidics* **2013**, *7*, 044113. [CrossRef] [PubMed]
20. Du, H.; Lu, D.; Qi, J.; Shen, Y.; Yin, L.; Wang, Y.; Zheng, Z.; Xiong, T.J. Heat dissipation performance of porous copper with elongated cylindrical pores. *Mater. Sci. Technol.* **2014**, *30*, 934–938. [CrossRef]
21. Toberer, E.S.; Seshadri, R. Template-free routes to porous inorganic materials. *Chem. Commun.* **2006**, *30*, 3159–3165. [CrossRef] [PubMed]
22. Shoemaker, D.P.; Corr, S.A.; Seshadri, R. Porosity through reduction in metal oxides. *Mater. Res. Soc. Symp. Proc.* **2008**, *1148*, 106–113. [CrossRef]
23. Marano, E.F.; Lussana, D.; Castellero, A.; Baricco, M. Nanoporous Microtubes obtained from a Cu-Ni Metallic Wire. *Met. Mater. Int.* **2016**, *22*, 305–310. [CrossRef]
24. Thermo-Calc Software. Available online: www.thermocalc.com (accessed on 30 September 2016).
25. Material Analysis Using Diffraction. Available online: http://maud.radiographema.com (accessed on 15 September 2016).
26. Pilling, N.B.; Bedworth, R.E. Oxidation of Copper-Nickel Alloys at High Temperatures. *Ind. Eng. Chem.* **1925**, *17*, 372–376. [CrossRef]
27. Sartell, J.A.; Bendel, S.; Johnston, T.L.; Li, C.H. The effect of oxide recrystallization on the oxidation kinetics of a 62:38 copper-nickel alloy. *Trans. Am. Soc. Met.* **1958**, *50*, 1047–1062.
28. Sartell, J.A.; Li, C.H. The oxidation of high-purity copper-nickel alloys. *Trans. Am. Soc. Met.* **1962**, *55*, 158–168.
29. Wagner, C.J. Theoretical analysis of the diffusion processes determining the oxidation rate of alloys. *Electrochem. Soc.* **1952**, *99*, 369–380. [CrossRef]
30. Whittle, D.P.; Wood, G.C. Two-phase scale formation on Cu-Ni alloys. *Corros. Sci.* **1968**, *8*, 298–308. [CrossRef]
31. MacDougall, B.; Cohen, M.J. Anodic Oxidation of Nickel in Neutral Sulfate Solution. *Electrochem. Soc.* **1974**, *121*, 1152–1159. [CrossRef]
32. Schmahl, N.G.; Barthel, J.; Eikerling, G.F. Röntgenographische Untersuchungen an den Systemen MgO−CuO und NiO−CuO. *Z. Anorg. Allg. Chem.* **1964**, *332*, 230–237. [CrossRef]
33. Eric, H.; Timuçin, M. Equilibrium relations in the system nickel oxide-copper oxide. *Metall. Trans. B* **1979**, *10*, 561–563. [CrossRef]
34. Cao, Z.-Q.; Niu, Y.; Gesmundo, F. Air oxidation of Cu-50Ni and Cu-70Ni alloys at 800 °C. *Trans. Nonferr. Met. Soc. China* **2001**, *11*, 499–502.
35. Smigelskas, A.D.; Kirkendall, E.O. Zinc diffusion in alpha brass. *Trans. AIME* **1947**, *171*, 130–142.
36. Weissmüller, J.; Newman, R.C.; Jin, H.-J.; Hodge, A.M.; Kysar, J.W. Nanoporous Metals by Alloy Corrosion: Formation and Mechanical Properties. *MRS Bull.* **2009**, *34*, 577–586. [CrossRef]
37. Newman, R.C.; Corcoran, S.G.; Erlebacher, J.; Aziz, M.J.; Sieradzki, K. Alloy corrosion. *MRS Bull.* **1999**, *24*, 24–28. [CrossRef]

© 2017 by the authors; licensee MDPI, Basel, Switzerland. This article is an open access article distributed under the terms and conditions of the Creative Commons Attribution (CC BY) license (http://creativecommons.org/licenses/by/4.0/).